Phonon scattering effects from point and extended defects on thermal conductivity studied via ion irradiation of crystals with self-impurities

Ethan A. Scott,[1] Khalid Hattar,[2] Christina M. Rost,[3] John T. Gaskins,[1] Mehrdad Fazli,[1] Claire Ganski,[4] Chao Li,[4] Tingyu Bai,[4] Yekan Wang,[4] Keivan Esfarjani,[1] Mark Goorsky,[4] and Patrick E. Hopkins[1,3,5]

[1]*Department of Mechanical and Aerospace Engineering, University of Virginia, Charlottesville, Virginia 22904, USA*

[2]*Sandia National Laboratories, Albuquerque, New Mexico 87185, USA*

[3]*Department of Material Science and Engineering, University of Virginia, Charlottesville, Virginia 22904, USA*

[4]*Materials Science and Engineering, University of California Los Angeles, Los Angeles, California 90095, USA*

[5]*Department of Physics, University of Virginia, Charlottesville, Virginia 22904, USA*

(Received 21 January 2018; revised manuscript received 23 July 2018; published 17 September 2018)

Fundamental theories predict that reductions in thermal conductivity from point and extended defects can arise due to phonon scattering with localized strain fields. To experimentally determine how these strain fields impact phonon scattering mechanisms, we employ ion irradiation as a controlled means of introducing strain and assorted defects into the lattice. In particular, we observe the reduction in thermal conductivity of intrinsic natural silicon after self-irradiation with two different silicon isotopes, $^{28}Si^{+}$ and $^{29}Si^{+}$. Irradiating with an isotope with a nearly identical atomic mass as the majority of the host lattice produces a damage profile lacking mass impurities and allows us to assess the role of phonon scattering with local strain fields on the thermal conductivity. Our results demonstrate that point defects will decrease the thermal conductivity more so than spatially extended defect structures assuming the same volumetric defect concentrations due to the larger strain per defect that arises in spatially separated point defects. With thermal conductivity models using density functional theory, we show that for a given defect concentration, the type of defect (i.e., point vs extended) plays a negligible role in reducing the thermal conductivity compared to the strain per defect in a given volume.

DOI: 10.1103/PhysRevMaterials.2.095001

I. INTRODUCTION

Crystalline imperfections in an otherwise perfect lattice generally create additional phonon scattering mechanisms that directly impact the thermal conductivity of solids. Specific phonon-defect scattering mechanisms and their impact on thermal conductivity have been studied for decades, stemming back to Klemens' work on phonon scattering with static lattice impurities [1]. According to Fermi's golden rule, interactions with point or line defects will lead to a change in crystal momentum and phonon scattering rates proportional to $A\omega^2 D_\omega$ or $A\omega D_\omega$, respectively, where ω is the phonon angular frequency, D_ω is the phonon density of states at frequency ω, and A is a proportionality constant related to the concentration, mass, and lattice strain associated with that defect [2]. In general, ample experimental works have studied and validated scattering theories regarding these phonon defect thermal resistances at macro- and nanoscales [1–10]. In materials with defects that have well defined masses (e.g., the different masses in solid solutions) or geometries (e.g., nanoparticle composites), the role of these masses and geometries on phonon scattering theories and A, its proportionality constant, can be quantitatively validated. However, deconvolving the role of strain in phonon scattering without the influence of the mass perturbation from the defect core to the lattice is a much bigger challenge. For example, interstitial point defects with atomic masses different than those of the host lattice will lead to phonon impurity scattering driven by both the mass differences and local strain around the interstitial [1,11–13]. Experimental studies that quantify and assess the impact of this local atomic-scale strain effect and the resulting phonon thermal conductivity would thus greatly enhance our understanding of phonon defect interactions.

Our goal in this work is to study the role of local atomic strain from defects on phonon scattering and the thermal conductivity of crystals. We use ion irradiation to systematically study how the thermal conductivity of silicon is impacted from strain induced by point and spatially extended defects. In general, ion irradiating solids leads to a decrease in their thermal conductivities due to increased phonon scattering with crystalline imperfections. Figure 1 displays a swath of various data from the literature [14–17] consisting of measured thermal conductivities at room temperature of different crystals as a function of dose of various ions. Ion implantation presents a unique tool to study phonon-defect effects in solids, and these thermal conductivity measurements presented in Fig. 1 demonstrate that varying irradiation conditions can drive relatively large changes in thermal conductivity. In this study, we irradiate natural silicon with Si isotopes, $^{28}Si^{+}$ and $^{29}Si^{+}$. The mass difference between the silicon host and the Si isotope is negligible, leading to reductions in thermal conductivity driven by lattice disorder induced from strain fields. These data are also shown in Fig. 1 where Si implanted with $^{28}Si^{+}$ is represented as filled diamonds and $^{29}Si^{+}$ as open diamonds. We attribute the different thermal conductivities between the $^{28}Si^{+}$ and $^{29}Si^{+}$ sample sets to the strain fields resulting from different densities of spatially extended and localized (i.e., point) defects from

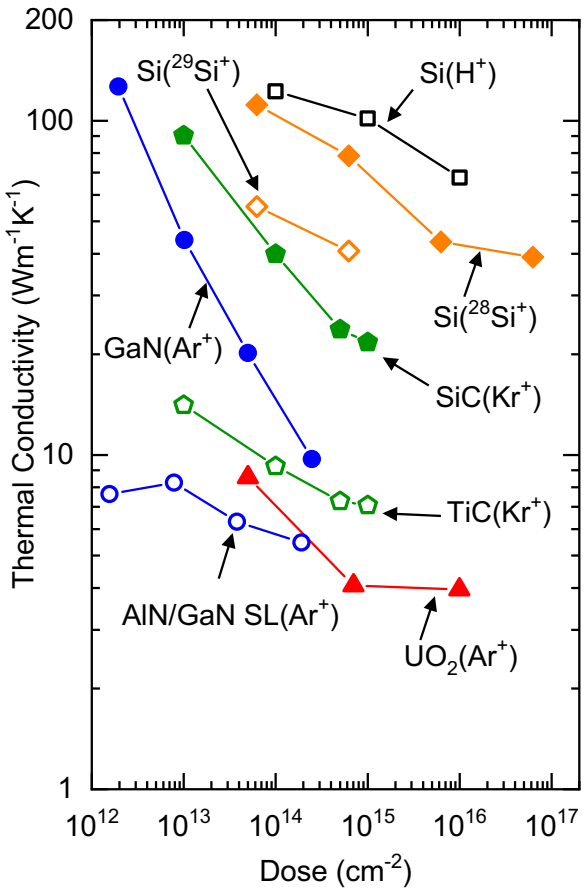

FIG. 1. Room temperature thermal conductivity of materials irradiated with various beam energies and ion species. The filled and unfilled orange diamond shapes are silicon irradiated with $^{28}Si^{+}$ and $^{29}Si^{+}$ ions, respectively, at 3.75 MeV (this work). The unfilled black squares are the thermal conductivity of silicon irradiated with protons at a beam energy of 200 keV [15]. The filled and unfilled green pentagons are SiC and TiC samples, respectively, irradiated with Kr^{+} ions at 74 MeV [14]. The filled and unfilled blue circles are GaN and AlN/GaN superlattice samples, respectively, irradiated with Ar^{+} ions at 2.3 MeV [17]. The red triangles display the thermal conductivity of UO_2 irradiated with Ar^{+} with a beam energy of 2 MeV (measurement taken at 328 K) [16].

the irradiation conditions, as confirmed with high-resolution x-ray diffraction (HRXRD) and high-resolution transmission electron microscopy (HRTEM). Our results demonstrate that point defects will decrease the thermal conductivity more so than spatially extended defect structures, assuming the same volumetric defect concentrations, due to the larger strain per defect that arises in spatially separated point defects. We implement thermal conductivity modeling using density functional theory (DFT) to show that, for a given defect concentration, the type of the defect (i.e., point vs line) plays a negligible role in reducing the thermal conductivity compared to the strain per defect in a given volume. This has direct implications to interpretations of reductions in thermal conductivity observed in nanocomposites with nanoparticles embedded in host materials [18–21], specifically addressing the role of strain in manipulating the thermal conductivity of materials. These results will significantly advance our understanding of phonon scattering in materials ranging from nano- to bulk scales.

II. SAMPLE FABRICATION

We implanted intrinsic (100) silicon wafers of thickness 400 μm from WRS Materials with silicon ions at Sandia National Laboratories using the 6 MV Tandem Van de Graaff Pelletron Accelerator. Wafers were cleaved into individual samples approximately 1 cm^2 in area. The first set of samples was irradiated using $^{28}Si^{+}$ ions at doses of 6.24×10^{13}, 6.24×10^{14}, 6.24×10^{15}, and 6.24×10^{16} cm^{-2} with a beam energy of 3.75 MeV. The second set was irradiated using $^{29}Si^{+}$ isotopes at doses of 6.24×10^{13}, and 6.24×10^{14} cm^{-2} at the same beam energy. Higher doses of $^{29}Si^{+}$ irradiation, namely 6.24×10^{15} and 6.24×10^{16} cm^{-2}, offered significant challenges during the irradiation process as $^{29}Si^{+}$ is an uncommon natural isotope and, thus, higher dose samples were unable to be fabricated. The beam was rastered across the sample surfaces to ensure uniform ion implantation. Simulations using SRIM software [22] were used to predict the damage profile within the samples, including two detailed calculations with full damage cascades. For the first, we designated the ion type as Si with a mass of 28 amu using a beam energy of 3.75 MeV. For the second case, the ion mass was increased to 29 amu with all other parameters held constant. The two simulations estimated the total number of induced target vacancies as 6131 and 6311 vacancies/ion, respectively. The depth of highest defect concentration was predicted to occur approximately 2.5 μm and the end of range at 3 μm beneath the sample surface, as shown in Fig. 2.

III. RESULTS

Following irradiation, samples were cleaned with alcohol (sonicated for five minutes in isopropanol, acetone, then methanol) and subjected to a thirty-minute O_2 plasma clean to remove organic contaminants [23–25]. The samples were then coated with an aluminum layer of 80 nm nominal thickness via electron beam evaporation to facilitate thermal conductivity measurements via time-domain thermoreflectance (TDTR). In short, TDTR is a pump-probe technique that correlates the thermoreflectivity at the surface of the sample to surface temperature. Fine temporal resolution of thermal decay is enabled through an ultrafast pulsed laser as the heat source; we utilize a Ti:Sapphire laser with a repetition rate of 80 MHz and central wavelength of 800 nm (bandwidth of 10.5 nm). The thermal properties of the samples were measured using TDTR by fitting the ratio of the in-phase to out-of-phase lock-in signal to thermal model detailed in the literature [26–29]. In the thermal model, each layer of the sample is assigned three parameters: volumetric heat capacity (C), thermal conductivity (κ), and layer thickness (d). In between layers, thermal boundary conductance or Kapitza conductance (h) produces an additional unknown. In practice, analysis of the TDTR data allows for extraction of two parameters with a single measurement [15]. We assume a literature value [30] of 1.65 MJm^{-3} K^{-1} for the volumetric heat capacity of intrinsic silicon at 300 K, verify the aluminum coating thickness through profilometry, and treat the silicon

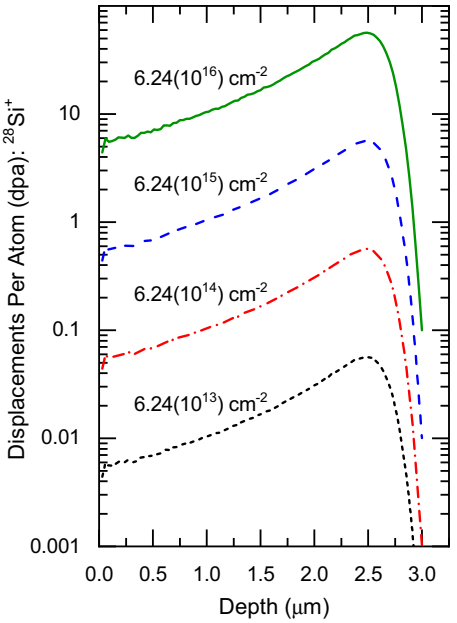

FIG. 2. SRIM output of the damage profile of Si irradiated with $^{28}Si^{+}$ ions at beam energy of 3.75 MeV. SRIM simulations were also conducted for $^{29}Si^{+}$ irradiated Si, yielding negligible differences in peak dpa depth and end of range depth. In both cases, the end of range is expected to occur around 2.5 μm from the sample surface. The total number of induced target vacancies was estimated to be 6131 and 6311 vacancies per ion for $^{28}Si^{+}$ and $^{29}Si^{+}$, respectively.

substrate as a semi-infinite medium, leaving thermal conductivity and thermal boundary conductance at the Al-Si interface as the only unknowns. The depth of ion implantation into the thickness of the samples is dependent upon beam energy [15]. Since both sample sets were implanted at 3.75 MeV, all samples have the same damage concentration profile, the magnitude of which is scaled according to the corresponding dose. To a first approximation, the depth of thermal penetration of the modulated pump-induced temperature gradient during a TDTR experiment is estimated as [31]

$$\delta = \sqrt{\frac{\kappa}{\pi C f}}, \tag{1}$$

where f is the modulation frequency of the pump beam. We caution that this expression for the thermal penetration depth is a rough approximation, as interfacial resistances and radial diffusion can lead to substantial deviations of the actual thermal penetration depth during TDTR [32,33]. However, the inverse dependence of δ with f holds true for the frequencies in this work; in other words, as we decrease the frequency, the thermal wave penetrates deeper in to the sample and hence we are able to resolve greater depths in the irradiated substrate. We modulate the pump at frequencies between 1 and 10 MHz, providing for a range of thermal penetration depths within the radiation-damaged region of interest. Using a modulation frequency of 10 MHz, in addition to a volumetric heat capacity of 1.65 $MJm^{-3}\,K^{-1}$, to a first approximation, thermal penetration depths on the order of 1.6 and 0.9 μm can be estimated for thermal conductivities of 140 and 40 $Wm^{-1}\,K^{-1}$, respectively, according to Eq. (1).

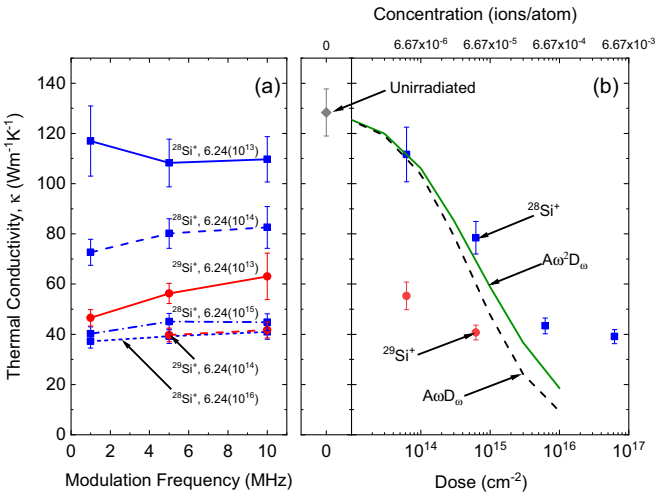

FIG. 3. The measured thermal conductivity of the irradiated Si as a function of modulation frequency is displayed in subfigure (a) for each irradiation dose. Samples implanted with $^{28}Si^{+}$ ions are shown in blue squares, whereas samples implanted with $^{29}Si^{+}$ ions are represented with red circles. In subfigure (b), the thermal conductivity values are averaged over the modulation frequency range to provide an average thermal conductivity for the damaged region of each sample and plotted as a function of dose. For comparison, the measured thermal conductivity of an unirradiated Si sample cleaved from the same wafer is also presented. First principles calculations of the thermal conductivity of silicon are plotted over of the measured thermal conductivity as a function of irradiation dose. The solid green line displays the reduction of thermal conductivity attributed to defects with an ω^4 scattering rate proportionality. The black dashed line shows the reduction attributed to defects with ω scattering rate proportionality. On the upper x axis, the ion concentration within the damaged region has been estimated from the dose by dividing the dose by the end of range (~3 μm as calculated from SRIM) and then dividing by the atomic density of silicon.

The same calculation with a modulation frequency of 1 MHz yields thermal penetration depths of 5.2 and 2.8 μm at $\kappa =$ 140 and 40 $Wm^{-1}\,K^{-1}$, respectively.

Figure 3(a) plots the measured thermal conductivity of the Si samples as a function of modulation frequency for each sample. The error bars are attributed to measurement repeatability as well as deviation in thermal conductivity as a result of uncertainty in aluminum thickness. In general, it can be seen that there is an overall increase in thermal conductivity with increased pump modulation frequency. This is expected as higher modulation frequencies yield shallower thermal penetration depths where the degree of damage is lower, as predicted by SRIM [15]. In general, it can be seen that there is overlap in the thermal conductivity uncertainty for a given sample as a function of frequency. Therefore, we average the thermal conductivities over the measured frequency range to find an average, representative thermal conductivity of the radiation damaged region. These averaged thermal conductivities are shown as a function of irradiation dose in Fig. 3(b). Both the $^{28}Si^{+}$ and $^{29}Si^{+}$ irradiated samples exhibit a reduction in thermal conductivity with increased ion dose, typical of the trend observed in irradiated solids (c.f., Fig. 1). In addition, there is a much larger reduction

in the thermal conductivity of the $^{29}Si^{+}$ irradiated samples as compared to the $^{28}Si^{+}$ irradiated samples.

IV. DISCUSSION

To understand the mechanisms driving these observed changes in silicon thermal conductivity with dose and isotope, it is instructive to consider the form of the phonon-defect scattering rates typically assumed in phonon thermal conductivity analyses. It is well known that the thermal conductivity of phonons is directly related to the spectrally integrated phonon scattering rate, which is related to all potential phonon scattering mechanisms via Matthiessen's rule, given by $\tau_{\omega}^{-1} = \tau_{\mathrm{Ph}}^{-1} + \tau_{\mathrm{Imp}}^{-1} + \tau_{\mathrm{Def}}^{-1}$, where τ_{Ph} represents phonon-phonon scattering processes (e.g., Umklapp and normal scattering), τ_{Imp} represents intrinsic impurity scattering (e.g., defects intrinsic to our wafers, such as natural isotopes), and τ_{Def} represents the additional scattering induced from the defects produced from the implantation conditions. Longstanding models for phonon-point defect scattering, originating with Klemens, suggest that [4,12]

$$\tau_{\mathrm{Def}}^{-1} = \frac{\omega^4 \delta^3 \Gamma_i}{4\pi v_{\omega}^3} \approx \Gamma_i \omega^2 D_{\omega}, \tag{2}$$

where δ^3 is the atomic volume (δ is the average lattice spacing) [4] and Γ_i characterizes the scattering cross section of the impurity i, defined as

$$\Gamma_i = x_i \left[\left(\frac{\Delta M_i}{M} \right)^2 + 2\left(\left(\frac{\Delta G_i}{G} \right) - 2 \times 3.2\gamma \left(\frac{\Delta \delta_i}{\delta} \right) \right)^2 \right], \tag{3}$$

which, for the purposes of our discussion in this work, we simplify to

$$\Gamma_i = x_i \left[\left(\frac{\Delta M_i}{M} \right)^2 + c\left(\Delta S_{G_i,\delta_i} \right)^2 \right]. \tag{4}$$

The term outside the brackets, x_i, is the impurity concentration. Within the brackets, the first term in Eq. (4) relates phonon scattering to the difference in impurity mass from the host crystal. The second term in Eq. (4), $c(\Delta S_{G_i,\delta_i})^2$, is directly related to the local strain per defect induced from the impurity mass, and is a function of several local properties of the host lattice and atoms around the defect site, including changes in the local bond stiffness and lattice constant changes ($\frac{\Delta G_i}{G}$ and $\frac{\Delta \delta_i}{\delta}$, respectively) and the Gruneisen parameter, γ. [1,4] Given that there is a negligible difference between the mass of the impurity and that of the host atoms in our Si samples, we can safely neglect the $\frac{\Delta M_i}{M}$ term in Eq. (4) for both the $^{28}Si^{+}$ and $^{29}Si^{+}$ case, which implies that local strain fields around the Si isotope are the primary source driving reduction in thermal conductivity.

As the difference in mass between these isotopes cannot explain the reduction in thermal conductivity when comparing the samples irradiated with $^{28}Si^{+}$ to those irradiated with $^{29}Si^{+}$, we turn to HRXRD and HRTEM to gain insight to the structural differences between these two samples sets. HRXRD was first used to quantify changes in the crystallinity of the silicon. Figure 4 plots the results of $\omega : 2\theta$ scans of all samples in addition to the control (unirradiated) sample, and focuses upon variations between the (400) planes. Scans performed in the $\omega : 2\theta$ geometry provide information on interplanar spacing along the direction perpendicular to the surface. As such, the formation of secondary peaks to the lower angle of the main peak is indicative of an increase in the interplanar spacing in this direction, which, in implanted single crystals, is attributed to the presence of a strained layer [34]. Rocking curves were also generated [Fig. 4(b)] in order to quantify the level of crystallinity. Again, focus was placed on the (400) peak. Defects, dislocations, and mosaicity all lead to deviations compared to an unirradiated sample [34], indicating an overall decrease in crystallinity. A simple means of quantifying this decrease is through calculation of the full width at half maximum (FWHM) of the rocking curve peaks (tabulated in Table I).

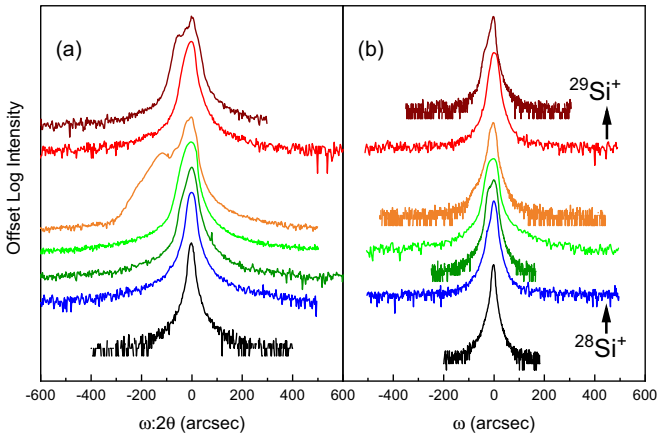

FIG. 4. HRXRD scans of the (400) peak for irradiated silicon samples in both (a) $\omega : 2\theta$ and (b) ω geometries. The bottom-most curve in each subfigure displays the control (unirradiated) sample. Corresponding to both subfigures, the arrow labeled $^{28}Si^{+}$ points to the sample irradiated with $^{28}Si^{+}$ with a dose of 6.24×10^{13} cm^{-2}, followed by 6.24×10^{14}, 6.24×10^{15}, and 6.24×10^{16} cm^{-2}, respectively. The arrow labeled $^{29}Si^{+}$ points to the sample irradiated with $^{29}Si^{+}$ with a dose of 6.24×10^{13} cm^{-2}, and above that, 6.24×10^{14} cm^{-2}.

In general, there is no systematic trend with increased dose, or from irradiating with a heavier ion. Increases in FWHM are seen in the $^{28}Si^{+}$ series as the dose increases from 6.24×10^{13} to 6.24×10^{15} cm^{-2}, but the FWHM decreases for the highest dose, 6.24×10^{16} cm^{-2}. In addition, there is no significant increase in FWHM between the $^{28}Si^{+}$ and $^{29}Si^{+}$ irradiated samples when comparing doses of 6.24×10^{13} and

TABLE I. FWHM calculations from the HRXRD rocking curves of Fig. 4(b).

Ion	Dose (cm^{-2})	FWHM (arcsec)
$^{28}Si^{+}$	6.24×10^{13}	11 ± 1
$^{28}Si^{+}$	6.24×10^{14}	22 ± 3
$^{28}Si^{+}$	6.24×10^{15}	24 ± 2
$^{28}Si^{+}$	6.24×10^{16}	15 ± 3
$^{29}Si^{+}$	6.24×10^{13}	15 ± 3
$^{29}Si^{+}$	6.24×10^{14}	13 ± 1

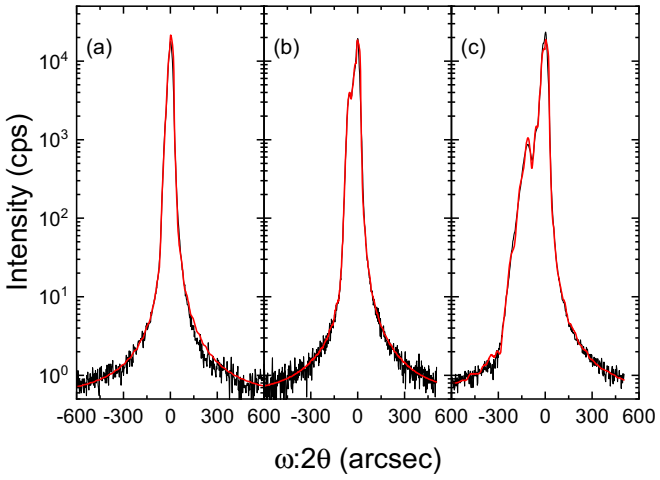

FIG. 5. RADS simulations plotted over top of experimental $\omega:2\theta$ scans. Subfigure (a) shows silicon irradiated with $^{28}Si^{+}$ to a dose of 6.24×10^{14} cm^{-2} and was found to have a maximum tensile strain of 150 ppm. Subfigure (b) shows silicon irradiated with $^{29}Si^{+}$ with the same dose and was found to have a strain of 280 ppm, and subfigure (c) shows silicon irradiated with $^{28}Si^{+}$ at the highest dose, and had a maximum tensile strain of 700 ppm.

6.24×10^{14} cm^{-2}. This lack of systematic increase in the FWHM of the rocking curves, in contrast to an increase in peak width in $\omega:2\theta$, is suggestive of an increase in interplanar spacing without an increase in mosaicity; this can be attributed to an increase in strain. For quantification of strain values, dynamical diffraction simulations were applied (Bruker RADS software [35]) to a number of the $\omega:2\theta$ curves, shown in Fig. 5. Simulations were performed to model the peaks for the $^{28}Si^{+}$ and $^{29}Si^{+}$ samples irradiated with a dose of 6.24×10^{14} cm^{-2}, as well as the $^{28}Si^{+}$ sample irradiated with the highest dose, 6.24×10^{16} cm^{-2}. For all samples, RADS simulations indicated that out-of-plane tensile strain existed within 3500 nm from the surface, which was in agreement with the damage profile calculated from SRIM (which predicted an end of range of 3 μm for both isotopes). For the $^{28}Si^{+}$ sample irradiated with a dose of 6.24×10^{14} cm^{-2}, the maximum tensile strains were calculated to be 150 ppm. For the $^{29}Si^{+}$ sample irradiated with the same dose, the maximum tensile strain was found to be 280 ppm. For the highest dose $^{28}Si^{+}$ irradiated sample, the maximum tensile strain was found to be 700 ppm.

For further characterization of structural changes within the irradiated samples, HRTEM was employed. Two samples were selected for analysis: silicon irradiated with $^{28}Si^{+}$ and $^{29}Si^{+}$ with a dose of 6.24×10^{14} cm^{-2}. Depths from 0.5–4 μm were analyzed. A Fourier-transform and inverse Fourier transform was performed on all TEM images with a filter added during image processing in order to increase the contrast of defects within the sample. The $^{28}Si^{+}$ sample exhibited the presence of extended defects from a depth of about 1 μm to 4 μm, whereas the $^{29}Si^{+}$ irradiated sample only showed defects at a depth of approximately 2.35 μm from the silicon surface, which closely corresponds to the projected range of the implant (in agreement with the dpa profile obtained from SRIM).

For the $^{28}Si^{+}$ irradiated samples, there was a factor of five increase in maximum tensile strain between samples subjected to a dose of 6.24×10^{14} and 6.24×10^{16} cm^{-2}, a lower ratio than what is to be expected, as linear increases of strain with dose have been previously observed [34]. It is known that implant-induced strain is reduced during annealing; the point defects that are initially present in the unannealed material can, upon annealing, coalesce into extended defects including dislocations, stacking faults, and twins [34,36]. As ^{28}Si is approximately 20 times more abundant than ^{29}Si, the rate of implantation, and therefore the temperature of the samples during implantation, could correspond. With faster implantation rates, higher temperatures can be expected and therefore defect clustering, dislocations, etc., would occur [37,38]. With a lower implantation temperature, the opposite would be expected: more point-defect sources. These concepts are supported in both the HRXRD and TEM analyses. While it is beyond the scope of this current work to identify why the different strain fields are generated during ion irradiation with different ion species, our HRTEM analysis demonstrates that the $^{28}Si^{+}$ sample displays a higher degree of extended defects, whereas the $^{29}Si^{+}$ irradiated sample contains more spatially localized defects, consistent with $^{29}Si^{+}$ irradiation generating a higher ratio of point defects and $^{28}Si^{+}$ irradiation tending towards spatially extended defects, such as defect clustering, dislocations, etc. (Fig. 6).

To gain further insight into the influence of strain within the samples, we model the thermal conductivity of silicon from a first-principles approach, described previously [39]. Calculations were performed for thermal conductivity as a function of A, the proportionality constant, as used in the phonon scattering rate, $A\omega^2 D_\omega$ and $A\omega D_\omega$ [2]. In the case of point defect strain scattering ($A\omega^2 D_\omega$), it can be seen that A is equivalent to Γ_i, the scattering cross section from the defect scattering rate in Eq. (3), which encompasses information about the local strain induced from the impurity. Therefore, $A=\Gamma_i=x_i c(\Delta S_{G_i,\delta_i})^2$. The impurity concentration, x_i, is a product of the dose as well as ion penetration depth and atomic density (as described in the caption of Fig. 3), which are constants, and therefore grouped into the constant coefficient term, c. Equation (4) can then be recast as $A=\Gamma_i=(DOSE)c'(\Delta S_{G_i,\delta_i})^2$, where c' is c with the aforementioned constants absorbed. With this, it is clear that the scaling term that relates the domain of the model, A, to that of the experimental data, $(DOSE)$, is $c'^{-1}(\Delta S_{G_i,\delta_i})^{-2}$. In the case of line defects, A is also related to the scattering strength, although the analytical form of this line defect coefficient is not as readily quantifiable as it is for point defects. The results of these calculations are shown along with our data in Fig. 3(b). It is readily apparent that the model is incapable of representing the thermal conductivity for either the $^{28}Si^{+}$ or $^{29}Si^{+}$ irradiated samples across the full dose range. In Fig. 7 we quantify the value of the scaling factor that would be needed to set the thermal conductivity found through first principles modeling equal to the experimentally measured thermal value for each dose and ion species. Because A is proportional to defect-induced strain, and since it must be scaled differently for each sample and dose, the strain must be adjusted for every sample and dose. This suggests that unique defect structures are created for each radiation condition; or

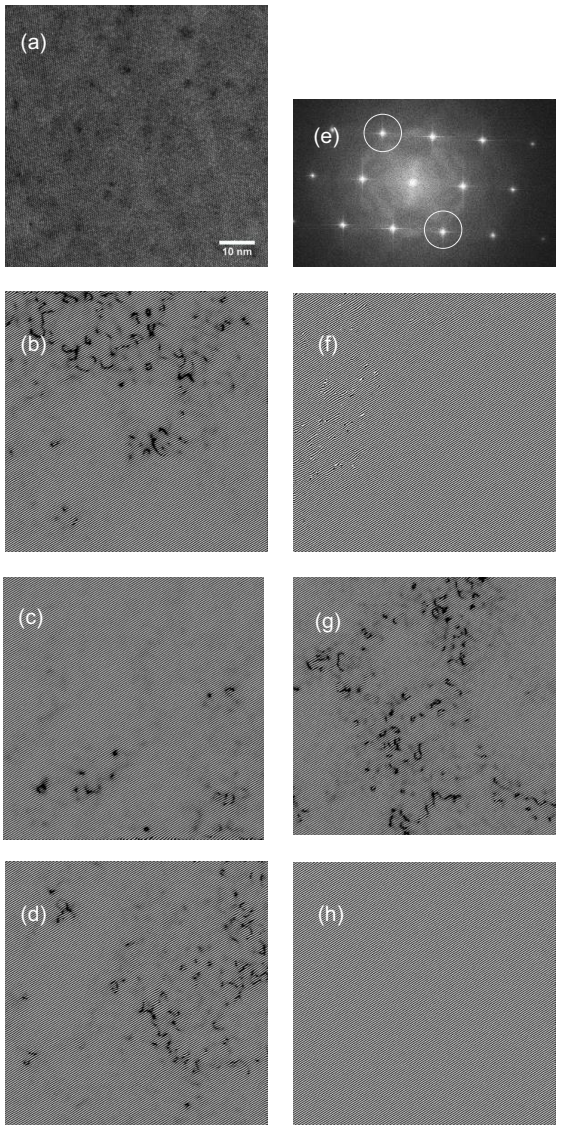

FIG. 6. HRTEM images of the irradiated silicon samples irradiated with a dose of 6.24×10^{14} cm^{-2}. Subfigure (a) displays an unfiltered image of $^{28}Si^{+}$ irradiated Si, centered at a depth of 1.01 μm. Subfigure (b) is the same image, filtered. Subfigures (c) and (d) display filtered images of $^{28}Si^{+}$ irradiated Si, centered at depths of 2.45 and 4 μm, respectively. Subfigure (e) displays the (200)/(2̄00) points that were selected for imaging. Subfigures (f)–(h) ($^{29}Si^{+}$ irradiated Si) display images centered at depths of 0.89, 2.35, and 4.02 μm, respectively.

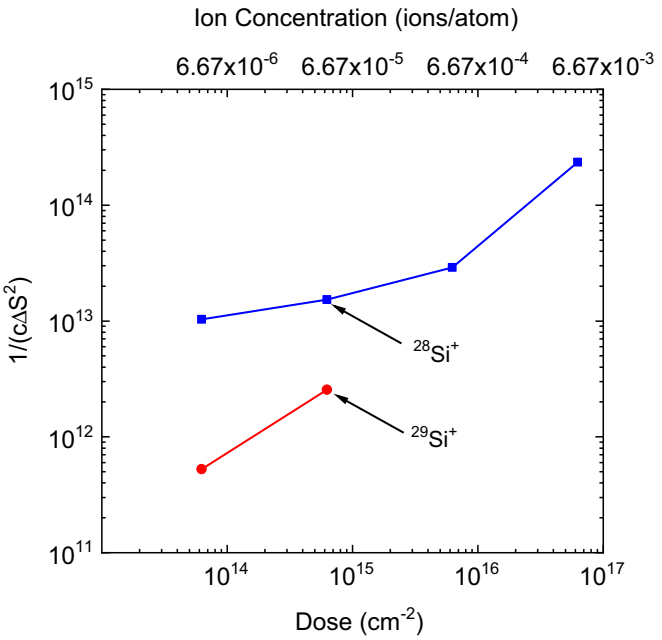

FIG. 7. Calculated scaling coefficients, $c'^{-1}(\Delta S_{G_i,\delta_i})^{-2}$, for each dose value such that the thermal conductivity calculated from the first principles model is set equal the measured values. The blue rectangles display data for the $^{28}Si^{+}$ irradiated samples, whereas the solid red circles display the same information for the $^{29}Si^{+}$ irradiated samples.

in other words, an increasing dose changes the strain fields around the defects. It is also noteworthy that the differences in the predictions of the models assuming either point or line defect scattering are negligible compared to the differences between the measured thermal conductivities of the $^{28}Si^{+}$ and $^{29}Si^{+}$ irradiated samples. This suggests that the type of defect (i.e., point vs line) plays a negligible role in reducing the thermal conductivity compared to the spatial extent of the strain field associated with that defect. From Fig. 7, it can be seen that for increasing dose values, the value of the scaling term increases. As the scaling term is inversely proportional to $\Delta S_{G_i,\delta_i}$, this suggests that the local strain per defect decreases as the dose increases. While this result may not be immediately intuitive, we note that the scattering cross-section formulation of Eq. (4) considers localized strain per defect [1,4] rather than global strain. As previously mentioned, $\Delta S_{G_i,\delta_i}$ is representative of the strain per defect, so even though there will be more overall global strain as the dose increases, our analysis suggests that the change in strain per defect will decrease with dose. HRXRD supports this finding, as it was shown that a two order of magnitude increase in dose only leads to only a factor of ≈4.6 increase in strain. In other words, although global strain increase as more ions are implanted into the lattice, the localized strain field per ion decreases, which can explained by the formation of extended defects, such as dislocations or vacancy clustering, dislocations, stacking faults, etc. [37,40–42], in agreement with the HRXRD and HRTEM findings.

V. SUMMARY

In summary, we report on the thermal conductivity of silicon substrates irradiated with two different isotopes of silicon, $^{28}Si^{+}$ and $^{29}Si^{+}$, measured via TDTR. The negligible mass difference between the implanted ion and the average mass of the substrate allows us to isolate the role of phonon-strain field scattering on the thermal conductivity. The type of isotope results in different spatial extents of the strain fields, consistent with point defects in the $^{29}Si^{+}$ irradiated samples and more extended defects in the $^{28}Si^{+}$ irradiated samples. Our results demonstrate that point defects will decrease the thermal conductivity more so than spatially extended defect structures assuming the same volumetric defect

concentrations due to the larger strain per defect that arises in spatially separated point defects.

ACKNOWLEDGMENTS

This material is based upon work supported by the Air Force Office of Scientific Research under award number FA9550-18-1-0352. The authors would like to thank D. Buller and R. Sisson with their assistance with the implantation, as well as the Nuclear Regulatory Commission for their support of this research through the Jump Start in Nuclear Materials Education and Research Graduate Fellowship Program at the University of Virginia. We also appreciate support from the Office of Naval Research under a MURI program, Grant No. N00014-18-1-2429. This work was performed, in part, at the Center for Integrated Nanotechnologies, an Office of Science User Facility operated for the U.S. Department of Energy (DOE) Office of Science. Sandia National Laboratories is a multimission laboratory managed and operated by National Technology and Engineering Solutions of Sandia, LLC., a wholly owned subsidiary of Honeywell International, Inc., for the U.S. DOE's National Nuclear Security Administration under contract DE-NA-0003525. The views expressed in the article do not necessarily represent the views of the U.S. DOE or the United States Government.

[1] P. G. Klemens, Proc. Phys. Soc. Sect. A **68**, 1113 (1955).
[2] G. Shrivastava, *The Physics of Phonons* (Taylor & Francis Group, LLC, New York, 1990), pp. 175–229.
[3] A. M. Marconnet, M. Asheghi, and K. E. Goodson, J. Heat Transfer **135**, 061601 (2013).
[4] B. Abeles, Phys. Rev. **131**, 1906 (1963).
[5] R. Cheaito, J. C. Duda, T. E. Beechem, K. Hattar, J. F. Ihlefeld, D. L. Medlin, M. A. Rodriguez, M. J. Campion, E. S. Piekos, and P. E. Hopkins, Phys. Rev. Lett. **109**, 195901 (2012).
[6] L. Wang, R. Cheaito, J. L. Braun, A. Giri, and P. E. Hopkins, Rev. Sci. Instrum. **87**, 094902 (2016).
[7] B. F. Donovan, B. M. Foley, J. F. Ihlefeld, J.-P. Maria, and P. E. Hopkins, Appl. Phys. Lett. **105**, 082907 (2014).
[8] B. M. Foley, H. J. Brown-shaklee, J. C. Duda, R. Cheaito, B. J. Gibbons, D. Medlin, F. Jon, P. E. Hopkins, B. J. Gibbons, D. Medlin, J. F. Ihlefeld, and P. E. Hopkins, Appl. Phys. Lett. **101**, 231908 (2012).
[9] D. G. Cahill and F. Watanabe, Phys. Rev. B **70**, 235322 (2004).
[10] D. G. Cahill, F. Watanabe, A. Rockett, and C. B. Vining, Phys. Rev. B **71**, 235202 (2005).
[11] B. F. Donovan, D. M. Long, A. Moballegh, N. Creange, E. C. Dickey, and P. E. Hopkins, Acta Mater. **127**, 491 (2017).
[12] B. F. Donovan, E. Sachet, J. P. Maria, and P. E. Hopkins, Appl. Phys. Lett. **108**, 021901 (2016).
[13] Y. K. Koh, C. J. Vineis, S. D. Calawa, M. P. Walsh, and D. G. Cahill, Appl. Phys. Lett. **94**, 153101 (2009).
[14] J. Cabrero, F. Audubert, P. Weisbecker, A. Kusiak, and R. Pailler, *Mechanical Properties and Performance of Engineering Ceramics and Composites IV* (John Wiley & Sons, Inc., Hoboken, 2010), pp. 205–217.
[15] R. Cheaito, C. S. Gorham, A. Misra, K. Hattar, and P. E. Hopkins, J. Mater. Res. **30**, 1403 (2015).
[16] P. B. Weisensee, J. P. Feser, and D. G. Cahill, J. Nucl. Mater. **443**, 212 (2013).
[17] Y. K. Koh, Y. Cao, D. G. Cahill, and D. Jena, Adv. Funct. Mater. **19**, 610 (2009); Y. K. Koh, M.-H. Bae, D. G. Cahill, and E. Pop, Nano Lett. **10**, 4363 (2010)
[18] A. Kundu, N. Mingo, D. A. Broido, and D. A. Stewart, Phys. Rev. B **84**, 125426 (2011).
[19] P. E. Hopkins, M. Mittal, L. M. Phinney, A. M. Grillet, and E. M. Furst, Appl. Phys. Lett. **99**, 133106 (2011).
[20] N. Mingo, D. Hauser, N. P. Kobayashi, M. Plissonnier, and A. Shakouri, Nano Lett. **9**, 711 (2009).
[21] W. Kim, J. Zide, A. Gossard, D. Klenov, S. Stemmer, A. Shakouri, and A. Majumdar, Phys. Rev. Lett. **96**, 045901 (2006).
[22] J. F. Ziegler, M. D. Ziegler, and J. P. Biersack, Nucl. Instrum. Methods Phys. Res., Sect. B **268**, 1818 (2010).
[23] P. E. Hopkins, K. Hattar, T. Beechem, J. F. Ihlefeld, D. L. Medlin, and E. S. Piekos, Appl. Phys. Lett. **98**, 231901 (2011).
[24] P. E. Hopkins, K. Hattar, T. Beechem, J. F. Ihlefeld, D. L. Medlin, and E. S. Piekos, Appl. Phys. Lett. **101**, 099903 (2012).
[25] C. S. Gorham, K. Hattar, R. Cheaito, J. C. Duda, J. T. Gaskins, T. E. Beechem, J. F. Ihlefeld, L. B. Biedermann, E. S. Piekos, D. L. Medlin, and P. E. Hopkins, Phys. Rev. B **90**, 024301 (2014).
[26] A. Schmidt, Optical characterization of thermal transport from the nanoscale to the macroscale, Dissertation, Massachusetts Institute of Technology, 2008.
[27] D. G. Cahill, Rev. Sci. Instrum. **75**, 5119 (2004).
[28] D. G. Cahill, K. E. Goodson, and A. Majumdar, J. Heat Transfer **124**, 223 (2002).
[29] P. E. Hopkins, J. R. Serrano, L. M. Phinney, S. P. Kearney, T. W. Grasser, and C. T. Harris, J. Heat Transfer **132**, 081302 (2010).
[30] P. Flubacher, A. Leadbetter, and J. Morrison, Philos. Mag. **4**, 273 (1959).
[31] Y. K. Koh, S. L. Singer, W. Kim, J. M. O. Zide, H. Lu, D. G. Cahill, A. Majumdar, and A. C. Gossard, J. Appl. Phys. **105**, 054303 (2009).
[32] J. L. Braun and P. E. Hopkins, J. Appl. Phys. **121**, 175107 (2017).
[33] J. L. Braun, C. J. Szwejkowski, A. Giri, and P. E. Hopkins, J. Heat Transfer **140**, 052801 (2018).
[34] M. Goorsky, *Ion Implantation*, edited by M. Goorsky (InTech, Rijeka, 2012), pp. 65–89.
[35] "Bruker Corporation, Karlsruhe, Germany, https://www.bruker.com/products/semiconductor-metrology/x-ray-metrology-for-compound-semiconductor/rads-software-bruker-semiconductor.html" (2018).
[36] J. Ziegler, Nucl. Instrum. Methods Phys. Res., Sect. B **6**, 270 (1985).

[37] P. D. Edmondson, An in-situ TEM study of the formation and annealing of the damage resulting from single ion impacts in crystalline silicon, Ph.D. thesis, The University of Salford, UK, 2007.

[38] R. M. Fleming, C. H. Seager, E. Bielejec, G. Vizkelethy, D. V. Lang, and J. M. Campbell, J. Appl. Phys. **107**, 053712 (2010).

[39] K. Esfarjani, G. Chen, and H. T. Stokes, Phys. Rev. B **84**, 085204 (2011).

[40] P. G. Coleman, J. Phys.: Conf. Ser. **265**, 012001 (2011).

[41] K. Gill, G. Hall, and B. MacEvoy, J. Appl. Phys. **82**, 126 (1997).

[42] S. Chakravarthi and S. T. Dunham, J. Appl. Phys. **89**, 4758 (2001).